

Observation of generalized Kibble-Zurek mechanism across a first-order quantum phase transition in a spinor condensate

L.-Y. Qiu, H.-Y. Liang, Y.-B. Yang, H.-X. Yang, T. Tian, Y. Xu, L.-M. Duan
Center for Quantum Information, IIIS, Tsinghua University, Beijing 100084, PR China

The Kibble-Zurek mechanism provides a unified theory to describe the universal scaling laws in the dynamics when a system is driven through a second-order quantum phase transition. However, for first-order quantum phase transitions, the Kibble-Zurek mechanism is usually not applicable. Here, we experimentally demonstrate and theoretically analyze a power-law scaling in the dynamics of a spin-1 condensate across a first-order quantum phase transition, when a system is slowly driven from a polar phase to an antiferromagnetic phase. We show that this power-law scaling can be described by a generalized Kibble-Zurek mechanism. Furthermore, by experimentally measuring the spin population, we show the power-law scaling of the temporal onset of spin excitations with respect to the quench rate, which agrees well with our numerical simulation results. Our results open the door for further exploring the generalized Kibble-Zurek mechanism to understand the dynamics across first-order quantum phase transitions.

Nonequilibrium dynamics across phase transitions plays a crucial role in various areas of physics ranging from cosmology to condensed matter [1]. At zero temperature, the properties of a quantum system are dictated by its ground state and the quantum phase transition is driven by quantum fluctuations. There, at the phase transition point, the energy gap vanishes and the relaxation time diverges, resulting in the violation of adiabaticity as the system parameter is tuned across the transition point. The Kibble-Zurek mechanism (KZM) describes the dynamics across the transition point by three evolution regions: two adiabatic and one impulse regions [2–8]. Specifically, when a system is far away from the transition point, the relaxation time is sufficiently short so that the system can respond to the change of a parameter and the dynamics is adiabatic. When the system is tuned to be near the point, it enters into an impulse region, where the relaxation time is sufficiently long so that the system cannot adapt to the change and thus remains frozen. After the impulse region, the energy gap becomes large and the system reenters into an adiabatic region. Based on the KZM, universal scaling laws are predicted across continuous quantum phase transitions for various quantities, such as topological defects and spin excitations. The KZM in quantum phase transitions has been experimentally observed in several systems [3, 9, 10, 12–16], such as Bose-Einstein condensates and a programmable Rydberg simulator.

Different from the second-order quantum phase transition, multiple phases coexist at the transition point for the first-order one. Interestingly, similar to the former, numerical simulations have suggested that scaling laws may also exist in the dynamics of several first-order phase transitions [17–21]. However, while the KZM is very successful in the former, some direct application of the KZM to the first-order transition cannot give a satisfied description of the scaling law compared to the numerical simulation results, such as in an extended Bose-Hubbard model [21]. In addition, there has been no experimental evidence for the existence of the scaling law at the first-order quantum phase transition.

A spinor Bose-Einstein condensate (BEC) provides a versatile platform to study the nonequilibrium physics, such as spin

domains [22–26], topological defects [27–30] and the KZM through the second-order phase transition [3]. The condensate is described by a vector order parameter. Under single-mode approximation, all spin states share the same spatial wave function so that the spin and spatial degrees of freedom are decoupled [2, 32]. For an antiferromagnetic (AFM) sodium condensate, its spin degrees of freedom exhibit a first-order quantum phase transition between an AFM phase with two $m_F = \pm 1$ levels equally populated and a polar phase with only the $m_F = 0$ level populated (m_F is the magnetic quantum number). This system therefore provides an ideal platform to explore the dynamics across the first-order quantum phase transition. Indeed, many interesting phenomena, such as coarsening dynamics of the instability [33], nematic and magnetic spin density waves [34], and dynamical phase transitions [35], have been experimentally observed in the spinor condensate.

In this paper, we theoretically and experimentally study the scaling law as a quadratic Zeeman energy is slowly varied from positive to negative values (or from negative to positive values) across the first-order quantum phase transition between the polar phase and the AFM phase. Our numerical simulation shows the existence of a power-law scaling of the temporal onset of the spin excitations with respect to the quench rate. Similar to the KZM at the continuous quantum phase transition, we find that the dynamics exhibit two adiabatic and one frozen evolution region, suggesting the existence of the KZM. For the KZM, the power-law scaling exponent is directly related to the scaling of the energy gap. For the conventional one, the scaling exponent is determined by the energy gap between the ground state and the first excited state. However, we find that this does not agree with our simulation result. We therefore generalize the KZM by considering the energy gap between the maximally occupied state (corresponding to the metastable phase) and its corresponding first excited state. Using this gap, we find that the predicted exponent agrees very well with our simulation result.

We further perform experiments in the sodium condensate to show the power-law scaling of the temporal onset of spin excitations with respect to the quench rate by measuring the

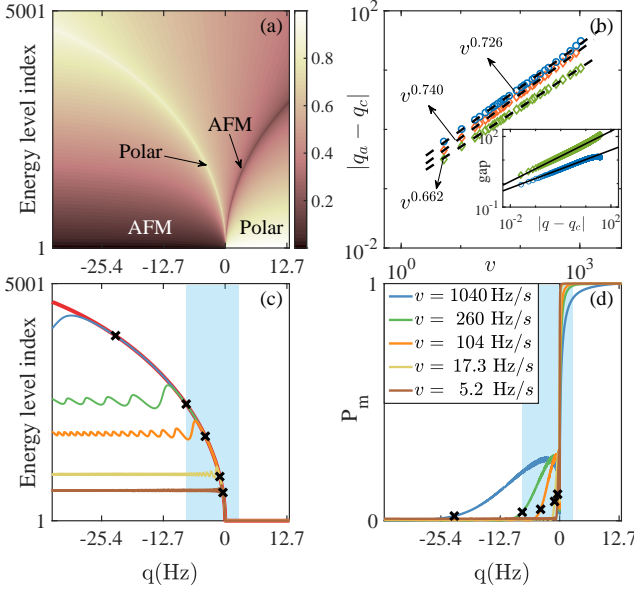


FIG. 1. (Color online) (a) $\langle \rho_0 \rangle$ for each energy level as a function of q . The existence of an AFM metastable state for $q > 0$ and a polar metastable state for $q < 0$ is observed. (b) The scaling of the q onset of the spin excitations q_a with respect to the quench rate v . Orange squares, green diamonds and blue circles are obtained by the numerical simulation, the KZM and the generalized KZM, respectively. The inset displays the scaling for the two gaps used in the KZM (green diamonds) and the generalized KZM (blue circles) with power-law fitting exponent of $\nu = 0.521$ and $\nu = 0.407$. (c) The evolution of the maximally occupied level $n_{\max}(t)$ for distinct v when q is varied from positive to negative values. The solid red line depicts the maximally occupied energy level n_{\max} for the initial state. This line coincides with the metastable polar phase as shown in (a). (d) The evolution of the probability on the maximally occupied level, i.e., $P_m = |\langle \psi_{n_{\max}}(q) | \psi(t) \rangle|^2$, for distinct v . In (c) and (d), the diagonal crosses label the position q_a where the spin excitations begin appearing, calculated by the numerical simulation. In (c) and (d), the filled light blue region shows the frozen region for $v = 260$ Hz/s, where the evolving state remains unchanged. We take $c_2 = 25.4$ Hz and the total atom number $N = 10000$ in the numerical simulation, with the energy level index of the Hamiltonian varying from 1, 2, \dots , 5001.

spin population. The experimental results agree well with our numerical simulations and the generalized KZM. Our result shows the first experimental evidence for the existence of the power-law scaling in the dynamics across the first-order quantum phase transition.

We start by considering a spinor BEC, which is well described by the following Hamiltonian under single-mode approximation

$$\hat{H}(q) = c_2 \frac{\hat{L}^2}{2N} + \sum_{m_F=-1}^1 (q m_F^2 - p m_F) \hat{a}_{m_F}^\dagger \hat{a}_{m_F}, \quad (1)$$

where \hat{a}_{m_F} ($\hat{a}_{m_F}^\dagger$) is the annihilation (creation) operator for the spin m_F component corresponding to the hyperfine level $|F = 1, m_F\rangle$, $L_\mu = \sum_{m,n} \hat{a}_m^\dagger (f_\mu)_{mn} \hat{a}_n$ is the condensate's total spin operator along μ with f_μ being the corresponding

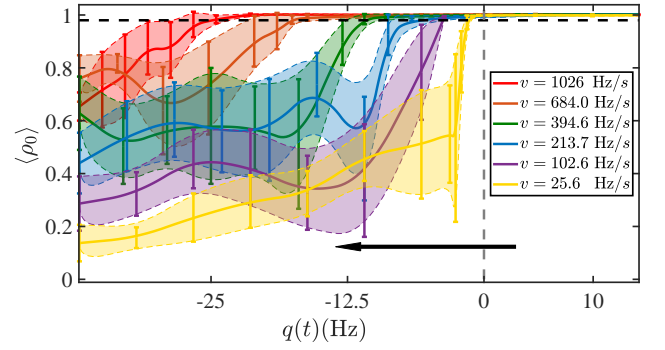


FIG. 2. (Color online) Experimentally measured mean value and standard deviation (denoted by the error bar) of ρ_0 , i.e., $\langle \rho_0 \rangle$ and $\Delta \rho_0$ with respect to $q(t)$ as $q(t)$ is slowly varied from positive to negative values for a number of ramp rates v with each point repeating 10 times. The horizontal and vertical dashed lines show the $\langle \rho_0 \rangle$ threshold and the phase transition point q_c , respectively. $\langle \rho_0 \rangle$ remains unchanged in the frozen region until at q_a when it begins to change, entering into the adiabatic region. Here, $c_2 = 25.5 \pm 1.5$ Hz.

spin-1 angular momentum matrix, c_2 is the spin-dependent interaction ($c_2 > 0$ for the antiferromagnetic sodium atoms), N is the total atom number and q (p) is the quadratic (linear) Zeeman energy.

In the absence of the linear Zeeman energy ($p = 0$), there are two phases for the ground state: a polar phase with atoms all occupying the $m_F = 0$ level for $q > 0$ and the AFM phase with atoms equally occupying the $m_F = \pm 1$ levels for $q < 0$ [32]. If we take mean value $\langle \rho_0 \rangle$ with $\rho_0 = \hat{a}_0^\dagger \hat{a}_0 / N$ as an order parameter, we can clearly see that $\langle \rho_0 \rangle$ abruptly drops from one to zero at $q = 0$, showing the first-order quantum phase transition there [see Fig. 1(a)]. At the transition point $q_c = 0$ Hz, these two phases coexist. In fact, near this point, we can observe the existence of the polar phase for $q < 0$ and AFM phase for $q > 0$ as metastable states, which is the characteristic of the first-order phase transitions. In real experiments, p is nonzero. However, since the Hamiltonian commutes with the total magnetization \hat{L}_z , i.e., $[\hat{H}(q), \hat{L}_z] = 0$, the quench dynamics is restricted in the subspace with zero magnetization if we prepare the initial state in the polar phase and the linear Zeeman term therefore becomes irrelevant.

To simulate the scaling in the dynamics across the first-order quantum phase transition, we start with the ground state of a spinor condensate in the polar phase for positive q_i and then linearly vary the quadratic Zeeman energy q by $q(t) = q_i - vt$ with $q_i > q_c$, $q_f < q_c$ and $v = (q_i - q_f)/\tau_q$ characterizing the quench rate with τ_q being the total time as q changes from q_i to q_f . To numerically simulate the dynamics, we solve the Schrödinger equation $i\hbar \partial |\psi(t)\rangle / \partial t = \hat{H}(t) |\psi(t)\rangle$ by directly diagonalizing the many-body Hamiltonian with Fock state basis $|N_{+1}, N_0, N_{-1}\rangle = \{|N/2, 0, N/2\rangle, |N/2 - 1, 2, N/2 - 1\rangle, \dots, |0, N, 0\rangle\}$. The time evolution of ρ_0 can be obtained by $\langle \rho_0 \rangle(t) = \langle \psi(t) | \rho_0 | \psi(t) \rangle$ for distinct v . Since the energy gap closes at the phase transition point, the system cannot adiabatically evolve with $\langle \rho_0 \rangle(t)$ unchanged. Thus, spin

excitations occur reflected by the decrease of $\langle \rho_0 \rangle(t)$ from one. Let t_a be the temporal onset of the spin excitations and $q_a = q(t = t_a)$ be the critical quadratic Zeeman energy at which the $\langle \rho_0 \rangle(t)$ begins to change. In Fig. 1(b), we show the presence of a power-law scaling for q_a with respect to the quench rate v (see the orange squares).

To delve into the reason underlying the presence of the scaling, let us show the presence of adiabatic and impulse evolution regions. As time progresses for distinct quench rates, we calculate the maximally occupied energy level of the evolved state defined as the $n_{\max}(t)$ th eigenstate $|\psi_{n_{\max}}(q)\rangle$ satisfying $|\langle \psi_{n_{\max}}(q) | \psi(t) \rangle| \geq |\langle \psi_n(q) | \psi(t) \rangle|$ for all n with $|\psi_n(q)\rangle$ being the eigenstate of $\hat{H}(q(t))$. Let us further define the maximally occupied energy level for the initial state as the n_{\max} th energy level that has the maximal overlap with the initial state, i.e., $|\langle \psi_{n_{\max}}(q) | \psi_0 \rangle| \geq |\langle \psi_n(q) | \psi_0 \rangle|$ for all n . This level coincides with the metastable polar phase with respect to q [see Fig. 1(a) and (c)], which is consistent with the first-order quantum phase transition. Interestingly, we find that when q is varied across zero, the former maximally occupied level $n_{\max}(t)$ rapidly increases by following the latter maximally occupied one n_{\max} as shown in Fig. 1(c), suggesting the existence of an impulse region where the state remains frozen. This can be seen from the fact that if the state remains in the initial state, its maximally occupied level for the evolving state is the same as the maximally occupied level for the initial state. In contrast, when the system leaves this region, the maximally occupied level $n_{\max}(t)$ begins approaching a fixed level, suggesting the presence of an adiabatic evolution. For instance, when $v = 260 \text{ Hz/s}$, the maximally occupied level $n_{\max}(t)$ follows n_{\max} inside the blue region and then converges to around the 2510th level in the long time limit [see the green line in Fig. 1(c)].

To further demonstrate the existence of impulse and adiabatic regions in the dynamics, we compute the evolution of the probability of atoms occupying the maximally occupied level, i.e., $P_m(q) = |\langle \psi_{n_{\max}}(q) | \psi(t) \rangle|^2$. As shown in Fig. 1(d), we find that the probability changes rapidly near the transition point, consistent with the prediction of an impulse evolution, and remains almost constant in other regions, consistent with the prediction of an adiabatic evolution. In addition, we mark out q_a as diagonal crosses determined by the numerical simulation, which agrees well with the q where the system leaves the impulse region and enters the adiabatic region [see Fig. 1(c-d)].

The presence of the impulse and adiabatic regions suggests that the scaling law may be accounted for by the KZM. Suppose that at $t = 0$, $q = q_c = 0$ and the system is in the polar phase. The q is then linearly varied by $q = -vt$. Based on the KZM, the critical time when the system begins to respond is determined by $\tau(t_a) = t_a$, where $\tau(t_a)$ is the relaxation time proportional to $1/\Delta E(t)$ with $\Delta E(t)$ being the energy gap near the transition point. We can also determine the critical time t_a by $1/|\Delta E(t)| = |\Delta E(t)/d\Delta E(t)/dt|$, after which the adiabaticity is restored. If the energy gap $\Delta E \propto |q - q_c|^\nu$ with ν being a positive real number, then the critical time is

given by $t_a \propto v^{-\nu/(\nu+1)}$ yielding $q_a \propto v^{1/(\nu+1)}$. This shows a power-law scaling of q_a with respect to v and the scaling exponent is determined by the energy gap. At the second-order phase transition, the relevant energy gap is the gap between the ground state and the first excited state labelled as ΔE_{12} . In our system, this energy gap $\Delta E_{12} \propto q^{1/2}$ contributed by the Bogoliubov spin excitations as $q \rightarrow 0$ [32]. This gives us $q_a \propto v^{2/3}$, consistent with our numerical result $q_a \propto v^{0.662}$ [see Fig. 1(b)]. It also tells us that the finite-size effects are very small when $N = 2 \times 10^4$ (see the Supplementary Materials for details about finite-size effects). However, at the first-order transition point, the numerical evolution gives us the exponent of 0.740, which is larger than the value predicted by the KZM by more than 10%. In stark contrast, if the energy gap is taken as the gap between the maximally occupied energy level, i.e., the n_{\max} th level and the corresponding first excited state relative to it, i.e., the $(n_{\max} + 1)$ th level, we find the exponent of 0.726, which agrees well with our numerical result. This is due to the different energy gap scaling as shown in the inset of Fig. 1(b). We call this method the generalized KZM. Yet, when we apply the generalized KZM to the second-order quantum phase transition, we find that the result is not as good as the one predicted by the first one, suggesting the difference between the first-order and second-order quantum phase transitions (see the Supplementary Materials for details about the KZM across the second-order quantum phase transition).

In experiments, we prepare a sodium BEC in the $3^2S_{1/2}$ [$F = 1$] hyperfine state by evaporation of atoms in an all-optical trap [35] and then apply a strong magnetic field gradient to kick the atoms on the $m_F = \pm 1$ levels out of the optical trap, leaving all atoms on the $m_F = 0$ level. After that, we hold the BEC atoms in a uniform magnetic field for 3 s to obtain a polar phase under the quadratic Zeeman energy of $q_B = 42 \text{ Hz}$ induced by the magnetic field. At the end of the holding, we turn on the microwave pulse with the frequency of 1.7701264 GHz (with the detuning of -1500 kHz from $|F = 1, m_F = 0\rangle$ to $|F = 2, m_F = 0\rangle$) to change the quadratic Zeeman energy to $q_i \simeq 15 \text{ Hz}$ (this time is defined as $t = 0$). Subsequently, we linearly vary the quadratic Zeeman energy from $q_i \simeq 15 \text{ Hz}$ to $q_f \simeq -38 \text{ Hz}$ by ramping up the amplitude of the microwave field. During the entire ramping time, we control the microwave power by a PID system according to the calibration of the quadratic Zeeman energy (see the Supplementary Materials for details about the q calibration). As time progresses, we apply the Stern-Gerlach fluorescence imaging to measure $\rho_0(t)$. At each time t , we repeat 15–20 measurements to obtain the average $\langle \rho_0 \rangle$ over the ensemble. Fig. 2 displays the observed $\langle \rho_0 \rangle$ as time evolves for a number of ramping rates v . The q_a is taken as the value when $\langle \rho_0 \rangle$ drops below 0.98. Evidently, q_a approaches zero as v is decreased.

To experimentally measure the power-law scaling, q_c should be precisely probed. We here employ the quench dynamics to identify the error of transitions point [35] in our calibration. Besides, we also employ the result to evaluate

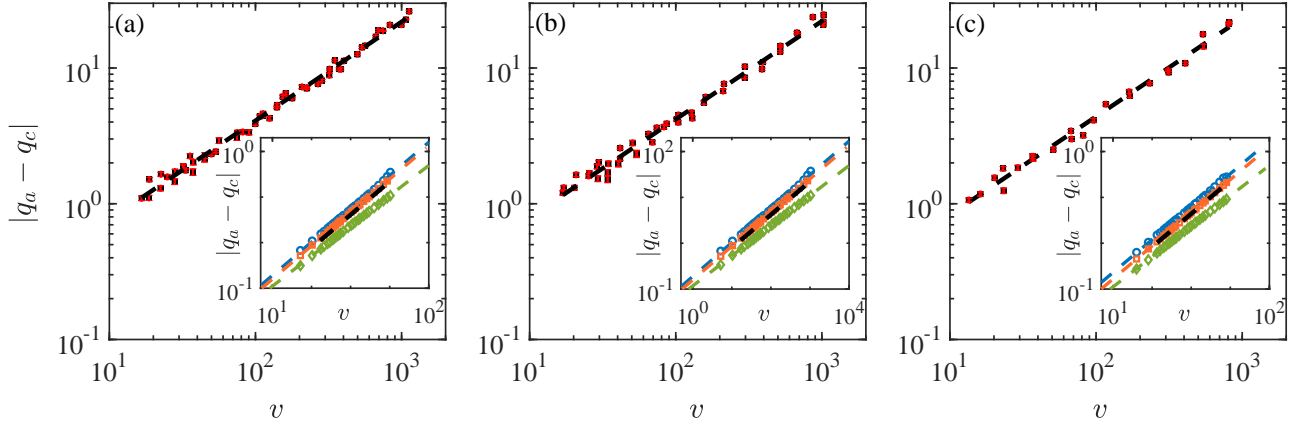


FIG. 3. (Color online) Experimentally observed scaling for $|q_a - q_c|$ with respect to the quench rate v shown in the logarithmic scale. In (a-b), q is tuned from around 15 Hz to around -38 Hz and in (c), from around -12 Hz to 28 Hz. In (a-c), $c_2 = 25.5 \pm 1.5$ Hz, $c_2 = 23.5 \pm 0.7$ Hz and $c_2 = 25.2 \pm 0.9$ Hz, respectively. The fitting of the experimental data shows the power-law scaling with the exponent of 0.728 ± 0.2 in (a), 0.723 ± 0.25 in (b) and 0.724 ± 0.32 in (c) with 95% confidence boundary. In the insets, we also plot the results of the numerical simulation (orange line), the KZM (green line) and the generalized KZM (blue line). For the numerical simulation, we take $N = 2.8 \times 10^4$ in (a), $N = 2.4 \times 10^4$ in (b), and $N = 2.6 \times 10^4$ in (c) associated with the corresponding c_2 . The experimentally observed exponents agree well with the exponents of 0.732 in (a), 0.735 in (b) and 0.723 in (c), which are obtained by the numerical calculation. The corresponding exponents predicted by the (generalized) KZM are 0.662 (0.731), 0.657 (0.738) and 0.662 (0.718), respectively. The error of $|q_a - q_c|$ arises from the onset time errors in experiments. For instance, if $\rho_0(t_1) > 0.98$ and $\rho_0(t_2) < 0.98$, we take $t_a = (t_1 + t_2)/2$ with the error of $t_1 - t_2$, leading to the error of q_a being $v(t_1 - t_2)$. In experiments, the error is smaller than 0.5 Hz and if $v < 52$ Hz/s, the error is smaller than 0.2 Hz.

the error of the v (see the Supplementary Materials for details about the q error evaluation).

In Fig. 3(a-b), we plot the observed $|q_a - q_c|$ with respect to v in the logarithmic scale, showing the existence of a power-law scaling, i.e., $|q_a - q_c| \propto v^\beta$. The fitting of the experimental data gives the exponent of $\beta = 0.728 \pm 0.2$ when $c_2 = 25.5 \pm 1.5$ Hz and $\beta = 0.723 \pm 0.25$ when $c_2 = 23.5 \pm 0.7$ Hz, which are slightly different for different c_2 due to the finite-size effect. The experimental results are also in good agreement with the numerical simulation results: $\beta = 0.732$ for the former and $\beta = 0.735$ for the latter (see the insets in Fig. 3). We also calculate the scaling law determined by the KZM and find that the exponents predicted by the generalized KZM are 0.731 for (a) and 0.738 for (b), which are closer to the simulation and the experimental results than the exponents of 0.662 and 0.657 predicted by the KZM. In addition, we find that the scaling is not sensitive to the atom loss as we can still observe it in the presence of 18% atom loss (see the Supplementary Materials for details about atom loss).

The scaling can also be observed when the system is driven from the AFM phase to the polar phase. In experiments, we prepare the initial state of the spinor BEC in a nearly AFM state by shining a $\pi/2$ -pulse radio frequency radiation to the BEC on the $|m_F = 0\rangle$ level. We then shine a resonant microwave pulse with the frequency of 1.7716264 GHz on the atoms for 300 ms to remove the remaining atoms on the $|m_F = 0\rangle$ level to obtain an AFM state. After that, we suddenly switch off this microwave pulse and switch on another one with the frequency of 1.7701264 GHz. By controlling the amplitude of a microwave field, we are able to linearly vary

the quadratic Zeeman energy from around -12 Hz to around 28 Hz. In Fig. 3(c), we show the experimentally measured relation between $|q_a - q_c|$ and v , illustrating a power-law scaling with the exponent of 0.724 ± 0.32 , which agrees very well with the numerical simulation result of 0.723 and the result of 0.718 predicted by the generalized KZM.

In summary, we have theoretically and experimentally studied the dynamics across the first-order quantum phase transition in a spin-1 condensate. We find the existence of a power-law scaling of the temporal onset of the spin excitations with respect to the quench rate. The scaling is well explained by the generalized KZM. We further perform an experiment to observe the power-law scaling by measuring the spin populations, which agrees well with the numerical simulation and the generalized KZM results. Our experiment is the first one to observe the scaling in the dynamics across the first-order quantum phase transition and hence opens an avenue for further studying universal scaling laws for first-order quantum phase transitions both theoretically and experimentally.

We thank Yingmei Liu, Ceren Dag, and Anjun Chu for helpful discussions. This work was supported by the Frontier Science Center for Quantum Information of the Ministry of Education of China, Tsinghua University Initiative Scientific Research Program, and the National key Research and Development Program of China (2016YFA0301902).

[1] A. Polkovnikov, K. Sengupta, A. Silva, and M. Vengalattore, Rev. Mod. Phys. **83**, 863 (2011).

- [2] T. W. Kibble, *Phys. Rep.* **67**, 183 (1980).
- [3] W. H. Zurek, *Nature* **317**, 505 (1985).
- [4] W. H. Zurek, *Acta Phys. Polon.* **24**, 1301 (1993).
- [5] W. H. Zurek, *Phys. Rep.* **276**, 177 (1996).
- [6] B. Damski, *Phys. Rev. Lett.* **95**, 035701 (2005).
- [7] W. H. Zurek, U. Dorner, and P. Zoller, *Phys. Rev. Lett.* **95**, 105701 (2005).
- [8] A. Polkovnikov, *Phys. Rev. B* **72**, 161201(R) (2005).
- [9] D. Chen, M. White, C. Borries, and B. DeMarco, *Phys. Rev. Lett.* **106**, 235304 (2011).
- [10] S. Braun, M. Friesdorf, S. S. Hodgman, M. Schreiber, J. P. Ronzheimer, A. Riera, M. Del Rey, I. Bloch, J. Eisert, and U. Schneider, *PNAS* **112**, 3641 (2015).
- [11] M. Anquez, B. A. Robbins, H. M. Bharath, M. Boguslawski, T. M. Hoang, and M. S. Chapman, *Phys. Rev. Lett.* **116**, 155301 (2016).
- [12] L. W. Clark, L. Feng, and C. Chin, *Science* **354**, 606 (2016).
- [13] J. Zhang, F. M. Cucchietti, R. Laflamme, and D. Suter, *New J. Phys.* **19**, 043001 (2017).
- [14] B. M. Anderson, L. W. Clark, J. Crawford, A. Glatz, I. S. Aranson, P. Scherpelz, L. Feng, C. Chin, and K. Levin, *Phys. Rev. Lett.* **118**, 220401 (2017).
- [15] S. Kang, S. W. Seo, J. H. Kim, and Y. Shin, *Phys. Rev. A* **95**, 053638 (2017).
- [16] A. Keesling, A. Omran, H. Levine, H. Bernien, H. Pichler, S. Choi, R. Samajdar, S. Schwartz, P. Silvi, S. Sachdev, *et al.*, *Nature* **568**, 207 (2019).
- [17] H. Panagopoulos and E. Vicari, *Phys. Rev. E* **92**, 062107 (2015).
- [18] I. B. Coulamy, A. Saguia, and M. S. Sarandy, *Phys. Rev. E* **95**, 022127 (2017).
- [19] A. Pelissetto and E. Vicari, *Phys. Rev. Lett.* **118**, 030602 (2017).
- [20] S. Kang, S. W. Seo, J. H. Kim, and Y.-i. Shin, *Phys. Rev. A* **95**, 053638 (2017).
- [21] K. Shimizu, T. Hirano, J. Park, Y. Kuno, and I. Ichinose, *New J. Phys.* **20**, 083006 (2018).
- [22] S. R. Leslie, J. Guzman, M. Vengalattore, J. D. Sau, M. L. Cohen, and D. M. Stamper-Kurn, *Phys. Rev. A* **79**, 043631 (2009).
- [23] M. Vengalattore, J. Guzman, S. R. Leslie, F. Serwane, and D. M. Stamper-Kurn, *Phys. Rev. A* **81**, 053612 (2010).
- [24] J. Kronjäger, C. Becker, P. Soltan-Panahi, K. Bongs, and K. Sengstock, *Phys. Rev. Lett.* **105**, 090402 (2010).
- [25] J. Guzman, G.-B. Jo, A. N. Wenz, K. W. Murch, C. K. Thomas, and D. M. Stamper-Kurn, *Phys. Rev. A* **84**, 063625 (2011).
- [26] C. V. Parker, L.-C. Ha, and C. Chin, *Nat. Phys.* **9**, 769 (2013).
- [27] L. Sadler, J. Higbie, S. Leslie, M. Vengalattore, and D. Stamper-Kurn, *Nature* **443**, 312 (2006).
- [28] L. S. Leslie, A. Hansen, K. C. Wright, B. M. Deutsch, and N. P. Bigelow, *Phys. Rev. Lett.* **103**, 250401 (2009).
- [29] J.-y. Choi, W. J. Kwon, and Y.-i. Shin, *Phys. Rev. Lett.* **108**, 035301 (2012).
- [30] J.-y. Choi, W. J. Kwon, M. Lee, H. Jeong, K. An, and Y.-i. Shin, *New J. Phys.* **14**, 053013 (2012).
- [31] Y. Kawaguchi and M. Ueda, *Phys. Rep.* **520**, 253 (2012).
- [32] D. M. Stamper-Kurn and M. Ueda, *Rev. Mod. Phys.* **85**, 1191 (2013).
- [33] E. M. Bookjans, A. Vinit, and C. Raman, *Phys. Rev. Lett.* **107**, 195306 (2011).
- [34] A. Vinit, E. M. Bookjans, C. A. R. Sá de Melo, and C. Raman, *Phys. Rev. Lett.* **110**, 165301 (2013).
- [35] H.-X. Yang, T. Tian, Y.-B. Yang, L.-Y. Qiu, H.-Y. Liang, A.-J. Chu, C. B. Dağ, Y. Xu, Y. Liu, and L.-M. Duan, *Phys. Rev. A* **100**, 013622 (2019).

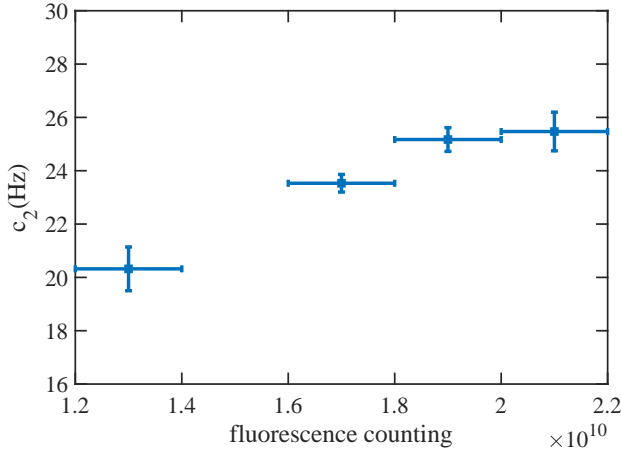


FIG. S1. Calibration of the spin-dependent interaction c_2 . The spin oscillation results of the mean value and standard deviation of c_2 , i.e. \bar{c}_2 and δc_2 versus the fluorescence counting number.

Supplemental Material

In the supplementary material, we will provide the detailed discussion on the calibration of the spin-dependent interaction c_2 in Section I, the calibration of the quadratic Zeeman energy q in Section II, the effects of atom loss in Section III, the finite-size effects in Section IV and the KZM across the second-order quantum phase transition in Section V.

Calibration of the spin-dependent interaction c_2

The calibration of the spin-dependent interaction parameter c_2 in our experiments is achieved by applying a widely used spin oscillation procedure as detailed in the following.

In experiments, we first prepare the BECs in the polar state with all atoms occupying the $m_F = 0$ level and then apply a radio frequency radiation to create a coherent state with $\langle \rho_0 \rangle = 1/2$ and $\langle \rho_{\pm 1} \rangle = 1/4$ under a magnetic field, which contributes a quadratic Zeeman energy of q_B . After that, the radio frequency radiation is switched off and the time evolution of the spinor condensates exhibits oscillations [1]. Since the period and amplitude of the oscillations are determined by c_2 and q_B , we can obtain c_2 by comparing the experimental results with the theoretical ones under a certain q_B with $q_B = q_z B^2$ where $q_z = 277 \text{ Hz}/G^2$.

Specifically, we measure the spin oscillation diagram under six different magnetic quadratic Zeeman energy q_B , and evaluate the mean value and standard deviation of c_2 , i.e., \bar{c}_2 and δc_2 with a narrow range of fluorescence counting number between a low limit N_L and a high limit N_H as shown by the fluorescence error bar in Fig. S1.

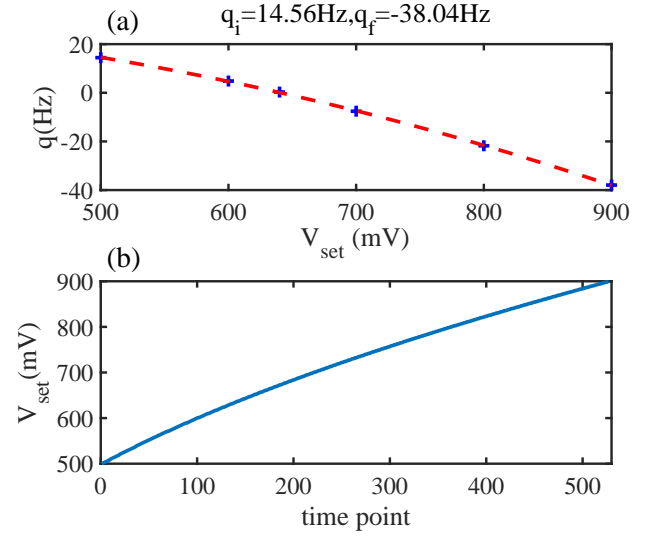


FIG. S2. The experimental power control of the microwave pulse. (a) The theoretically calculated q (blue crosses) based on the experimentally measured Rabi frequencies with respect to six different microwave power V_{set} : 500 mV, 600 mV, 640 mV, 700 mV, 800 mV, and 900 mV. The dashed line is the fitting of the six data by a parabola. In experiments, we control the V_{set} following the line in (b) as time progresses to achieve the linear ramping of q_i from $q_i = 14.56 \text{ Hz}$ to $q_f = -38.04 \text{ Hz}$. The total time point number is 500 and the τ_q is directly controlled by the time period of the ramping process.

Calibration of the quadratic Zeeman energy q

To calibrate the quadratic Zeeman energy q , we measure the Rabi frequency of $\sigma+$, π , $\sigma-$ transitions under a PID microwave power control system in experiments. We also apply the quench dynamics method to evaluate the error in the calibration process of q .

In our experiments, the quadratic Zeeman energy is given by $q = q_B + q_M$, where q_B and q_M are generated by the magnetic field and microwave pulse, respectively. The magnetic Zeeman energy q_B is about 42 Hz in the whole ramping period. The microwave Zeeman energy is given by

$$q_M = \frac{\delta E_{m_F=+1} + \delta E_{m_F=-1} - 2\delta E_{m_F=0}}{2}, \quad (\text{S1})$$

where

$$\begin{aligned} \delta E_{m_F} &= \frac{\hbar}{4} \sum_{k=-1,0,+1} \frac{\Omega_{m_F \rightarrow m_F+k}^2}{\delta_0 - [(m_F+k)g_F - (-m_F)g_F]\mu_B B} \\ &= \frac{\hbar}{4} \sum_{k=-1,0,+1} \frac{\Omega_{m_F \rightarrow m_F+k}^2}{\delta_0 - [(m_F+k)g_F - (-m_F)g_F]\mu_B B} \end{aligned} \quad (\text{S2})$$

with $\Omega_{m_F \rightarrow m_F+k}$ being the resonant Rabi frequency for the transition from $|F=1, m_F\rangle$ to $|F=2, m_F+k\rangle$ and δ_0 being the microwave detuning for the transition from $|F=1, m_F=0\rangle$ to $|F=2, m_F=0\rangle$.

In experiments, we measure the three Rabi frequencies of $\sigma+$, π and $\sigma-$ transitions corresponding to $\Omega_{m_F=0 \rightarrow m_F=1}$,

PID	$V_{\text{set}}(\text{mV})$	$\overline{q_1}(\text{Hz})$	$\delta q_1(\text{Hz})$	$\overline{q_2}(\text{Hz})$	$\delta q_2(\text{Hz})$
	500	0.034	0.355	-0.082	0.357
	600	-0.088	0.393	-0.182	0.393
	640	0.162	0.176	0.075	0.176
	700	0.280	0.400	0.203	0.402
	800	0.183	0.253	0.118	0.254
	900	0.068	0.229	0.005	0.230

TABLE I. The error evaluation of q . The mean value $\overline{q_{1,2}}$ and standard deviation $\delta q_{1,2}$ of $q_{1,2}$ based on the data in one month for distinct V_{set} .

$\Omega_{m_F=-1 \rightarrow m_F=-1}$ and $\Omega_{m_F=0 \rightarrow m_F=-1}$, respectively, and then determine the q_M based on the above formula. The detuning of the microwave pulse δ_0 is precisely controlled by the Keysight E8663D PSG RF Analog Signal Generator. Without a PID system, its power requires more than 1 s to reach a stable value (after the RF amplifier ZHL-30W-252-S+), causing an error of q about -3 Hz. We therefore apply a PID system to shorten the time for the microwave power to reach a set value V_{set} to less than $100\mu\text{s}$. The Rabi frequencies are measured during $130\mu\text{s} - 300\mu\text{s}$ after the microwave pulse is switched on.

In Fig. S2, we plot the result of q based on the experimentally measured Rabi frequencies at six distinct V_{set} with frequency detuning $\delta_0 = -1500$ kHz. The figure also shows the fitting of these data by a parabola (see the dashed red line) and with this fitting line, the V_{set} is controlled following the line shown in Fig. S2(b) to realize the linear change of the q .

In the following, we apply the quench dynamics to measure the quantum phase transition point and evaluate the q calibration error. We first prepare the BECs in the polar phase under a positive q_i and then suddenly quench the q to q_f . If q_f is positive, the atoms remain on the $m_F = 0$ level after 500 ms evolution, and if q_f is negative, the atoms on the $m_F = \pm 1$ levels show up after 500 ms evolution. In experiments, $\langle \rho_0 \rangle$ is measured after this period of time for distinct V_{set} as the microwave frequency is suddenly tuned to ν_f . To find the transition point, we control the ν_f to find the minimum ν_1 so that $\langle \rho_0 \rangle$ remains unchanged and the maximum ν_2 so that $\langle \rho_0 \rangle$ is decreased. Note that the q decreases as the frequency ν_f is increased with δ_0 varying from -2000 kHz to -1300 kHz. For these two frequencies $\nu_{1,2}$, we calculate the quadratic Zeeman energy q_1 and q_2 , respectively, under the V_{set} .

In Table I, we show the mean value $\overline{q_{1,2}}$ and standard deviation $\delta q_{1,2}$ of $q_{1,2}$ based on the quench dynamics data in one month. The error of the q leads to the error of the v as $\delta v = \sqrt{\delta q_1(V_{\text{set}} = 500\text{mV})^2 + \delta q_1(V_{\text{set}} = 900\text{mV})^2} / \tau_q$, where $\delta q_1(V_{\text{set}} = 500\text{mV})$ and $\delta q_1(V_{\text{set}} = 900\text{mV})$ are the standard deviations for $V_{\text{set}} = 500\text{mV}$ and $V_{\text{set}} = 900\text{mV}$, respectively.

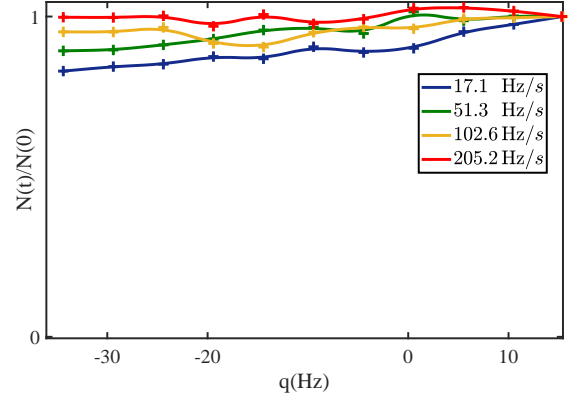


FIG. S3. Atom loss result. The amount of atoms loss for different ramping rates v reflected by the decline of the relative atom number $N(t)/N(0)$ when we control the microwave amplitude so that the q is linearly decreased. Here, $N(0)$ denotes the initial atom number.

The effects of atom loss

In experiments, atom loss occurs due to the microwave and optical radiation. In Fig. S3, we display the amount of atom loss for different quench rates, showing that the amount increases when the q is linearly decreased achieved by controlling the microwave amplitude and it also increases for smaller v . Specifically, when $v = 17.1$ Hz/s, which is the slowest quench rate in the experiments, the amount of atom loss is roughly 18% at the end of the ramp and 10% near the $q_c = 0$ Hz point. Despite the presence of atom loss, it does not have obvious effects on our measured scaling property as shown in Fig. 3 in the main text.

Finite-size effects

In Fig. S4, we plot the numerically calculated exponent β as a function of the atom number, showing that the exponent approaches a steady value of 0.75 as the atom number increases. We also show that the exponent is not quite sensitive to ρ_{0c} for large atom numbers. In our experiments, we take $\rho_{0c} = 0.98$.

The KZM across the second-order quantum phase transition

For rubidium atoms with negative c_2 , the condensate exhibits a second-order quantum phase transition at $q = 2c_2$ between a polar phase for $q > 2c_2$ and a broken-axisymmetry (BA) phase [2]. The scaling exponent predicted by the KMZ is $\beta = 2/3$, which has been experimentally observed using rubidium atoms [3]. This agrees well with our numerical simulation result of $\beta = 0.655$ under the parameters of $N = 2 \times 10^4$, $c_2 = -24.5$ Hz, $q_i = 70$ Hz and $q_f = 10$ Hz. However, the exponent predicted by the generalized KZM is $\beta = 0.801$, more than 20% larger than the numerical simu-

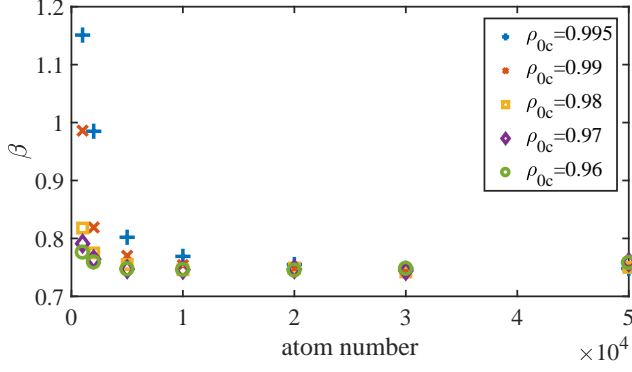


FIG. S4. Summary of β under different situation. The numerically calculated exponent β with respect to the number of atoms for different ρ_{0c} . Here, $c_2 = 20$ Hz, $q_i = 15$ Hz and $q_f = -50$ Hz.

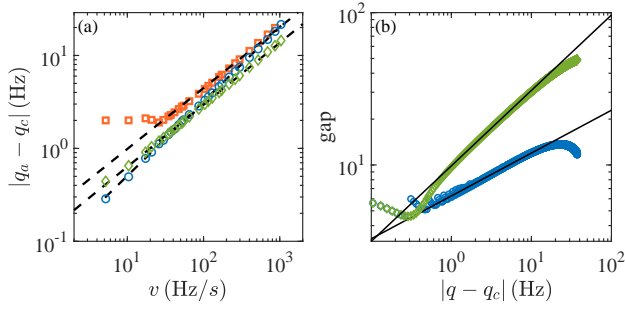


FIG. S5. The scaling law across a second-order quantum phase transition. (a) $|q_a - q_c|$ with respect to the quench rate v obtained by the numerical simulation (orange squares), the KZM (green diamonds) and the generalized KZM (blue circles), respectively. The dashed lines are the power-law fitting of these data, yielding the exponent of $\beta = 0.655$, $\beta = 0.668$ and $\beta = 0.801$, respectively. (b) The energy gap as a function of $|q - q_c|$. The power-law fitting gives the exponent of $\nu = 0.495$ and $\nu = 0.281$ for the energy gap (green diamonds) between the ground state and the first excited state and the energy gap (blue circles) between the maximally occupied state and the corresponding first excited state, respectively. Note that when $|q - q_c|$ is very small, the fitting is not good due to the finite-size effects creating a finite energy gap at $q = q_c$. Here, $N = 10^4$, $c_2 = -25.4$ Hz, $q_i = 65.3$ Hz, $q_f = 13.3$ Hz and $q_c = 2c_2$.

lation results, as shown in Fig. S5. This tells us that for the second-order quantum phase transition, the relevant energy gap is the gap between the ground state and the first excited state.

-
- [1] A. T. Black, E. Gomez, L. D. Turner, S. Jung, and P. D. Lett, Phys. Rev. Lett. **99**, 070403 (2007).
 - [2] Y. Kawaguchi and M. Ueda, Physics Reports **520**, 253 (2012).
 - [3] M. Anquez, B. Robbins, H. Bharath, M. Boguslawski, T. Hoang, and M. Chapman, Physical review letters **116**, 155301 (2016).